Signal reconstruction in the EM end-cap calorimeter and check with cosmic data in the region $0 < \eta < 3.2$

C. Gabaldon Ruiz, J. del Peso
Universidad Autonoma de Madrid (UAM)

F. Hubaut, M. Kuna, P. Pralavorio
Centre de Physique des Particules de Marseille, CNRS/IN2P3 - Univ. Méditerranée, Marseille - France

ATL-LARG-PUB-2008-001
26 March 2008

Abstract

In 2007, the electromagnetic end-cap calorimeter joined the ATLAS commissioning effort. Since then, calibration and cosmic muon runs are taken regularly, allowing to set-up, debug and test *in situ* the signal reconstruction. These are the first data in the $1.4 < \eta < 3.2$ region since 2001-2002 test beam period. The few % of cosmic events with catastrophic high energy deposits (typically $E > 500$ MeV) have been used to perform a systematic and quantitative comparison between data and predicted physics pulse shapes in a coherent way over the entire calorimeter coverage, $0 < \eta < 3.2$. This represents the first attempt to unify barrel and end-cap *in situ* data in a common analysis. Results are similar in the barrel and the end-cap, only slightly worse for the latter as expected from its more complex geometry. This is the first proof of the quality of an ATLAS-like signal reconstruction in the end-caps, despite its challenging aspect, and gives confidence that the energy reconstruction is in good control over the complete electromagnetic calorimeter coverage $0 < \eta < 3.2$.

Contents

1 Introduction

The EM calorimeter is installed in the ATLAS cavern since the end of 2006. Before the LHC start, the main challenge is to operate coherently its $\sim 170\,000$ channels, *i.e* commission the associated electronics, automate all calibration steps. A smooth reconstruction of the cosmic muon signals on the full calorimeter coverage ($|\eta| < 3.2$) would provide an outstanding result. The signal reconstruction method is based on an accurate knowledge of the electronic chain characteristics, that goes from the detector capacitance to the analog shaping in the front end electronics [1]. It has been developed and tuned with standalone [2, 3] and combined [4] beam test campaigns, but used and tested mainly on the barrel part.

Cosmic muons can provide a last test bench before the LHC start for this signal reconstruction procedure. They have already been used recently to partly commission the barrel part, leading to preliminary results on calorimeter uniformity along η and timing performance [5]. The rate of projective muons in the end-caps is too low to perform such studies. However, the use of catastrophic high energy deposits, occurring over the entire calorimeter coverage, can provide a complete cross-check of the reconstruction chain in a coherent way for both barrel and end-cap parts. This is the purpose of the present note. The end-cap part, much less tested so far, will have the main focus, and its results will be carefully compared to the barrel ones. This is particularly important as its geometry is more complicated, with the consequence that most electrical parameters vary by a factor $2-3$ over the end-cap η-coverage whereas they are almost constant in the barrel. This requires extensive cross-checks to avoid any systematic bias.

This note is organised as follows. Section 2 recalls briefly the main characteristics of the EM calorimeter and presents the specificities of its end-cap parts. Section 3 details the inputs needed for the signal reconstruction and estimates the calibration bias and the noise reduction linked to the method. Section 4 gives the results of the quality checks performed with the cosmic muon data. Finally, section 5 is dedicated to conclusions.

2 EM calorimeter and main end-cap specificities

The electromagnetic (EM) calorimeter is a lead-liquid argon (LAr) sampling calorimeter with an accordion geometry [6] that guarantees a full azimuthal coverage. It is divided in one barrel ($|\eta| < 1.475$) [7] and two end-caps ($1.375 < |\eta| < 3.2$) [8] and is segmented in depth in three compartments [1]. In total, around 170 000 read-out channels (101 760 in barrel, 62 208 in end-caps and 9 344 in presampler) give the detector a high granularity, recalled in Appendix 1. As illustrated in Figure 1, each of these cells can be modelled as a resonant *rLC* circuit, where *C* corresponds to the cell capacitance, *L* to the inductive path of the ionisation signal and *r* to the contact resistance between detector cell and readout line. These cell characteristics must be known precisely to control the quality of the signal reconstruction (section 3), as they are not accounted for by the calibration system, which only shares with physics signals the complete readout chain (where signals are amplified, shaped, sampled every 25 ns and digitized).

[1] The thin presampler detector correcting for the energy losses in the upstream material for $|\eta| < 1.8$ is not discussed in this note as no cosmic muon signals can be detected in.

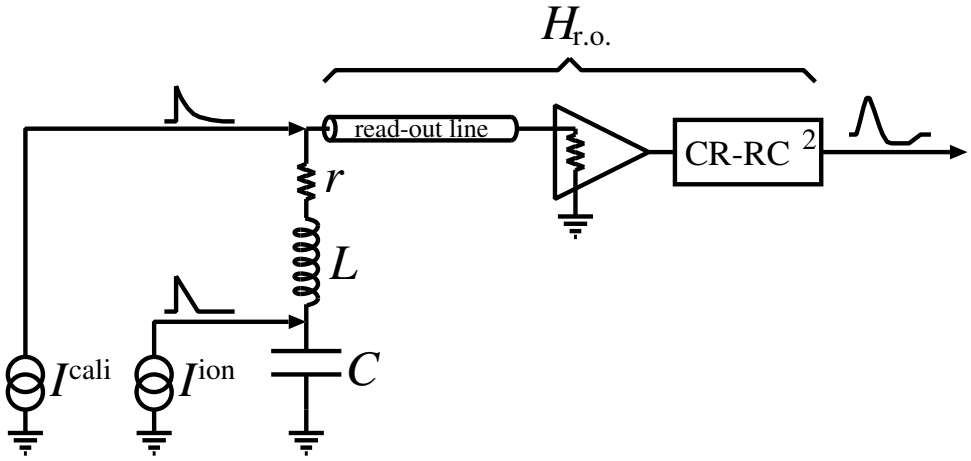

Figure 1: *Schematic electrical model of a LAr cell with its readout chain and calibration network. Shapes of calibration and ionisation signals are illustrated, as well as the output pulse.*

Both barrel (EMB) and end-cap (EMEC) parts of the EM calorimeter have an accordion geometry for absorbers and electrodes, and identical calibration and read-out electronics. However the choice of an accordion shape in the end-cap region induces a more complicated geometry [8]. First, the EMEC had to be divided in two wheels, called outer ($1.375 < |\eta| < 2.5$) and inner ($2.5 < |\eta| < 3.2$) wheels, both projective in η. Then, as outlined in Table 1, most of the design parameters vary smoothly along the radius direction (corresponding to η), typically by a factor $2-3$, whereas they are almost constant in the barrel [2] : liquid argon gap, accordion wave amplitudes, bending angles, etc. This is therefore also the case for the ion drift time in liquid argon and for the signal sampling fraction. To partially compensate for these variations, the high voltage is set by steps into several high voltage sectors (see Appendix 1). Finally, the variation of the cell electrical characteristics r, L and C is also important over the end-cap η-coverage. This will be detailed in the next section, where the implications on the signal reconstruction will be investigated.

	Barrel	End-caps
Gap (mm)	2.1	3.1 to 0.9
Bending angle ($^\circ$)	70 to 90	60 to 120
Drift time (ns)	470	600 to 200
dE/dX sampling fraction (%)	25 or 28	30 to 14
HV (V)	2000	2500 to 1000
S2 Cell inductance L (nH)	25 to 35	50 to 20
S2 Cell Capacitance at cold C (pF)	1400 or 1900	1200 to 600

Table 1: *Some geometrical and electrical characteristics of the barrel and end-cap outer wheel EM calorimeter. In the former case, parameters may vary at $|\eta| = 0.8$. In the latter case, the variation is smooth and given for increasing $|\eta|$ from 0 to 2.5.*

[2] Some barrel characteristics change at $|\eta| = 0.8$, due to the change of lead plate thickness.

3 Signal reconstruction in the end-caps

This section first introduces the basics of the signal reconstruction method foreseen for barrel and end-cap EM calorimeters, and then synthesises the present knowledge of the input parameters needed to compute the optimal filtering coefficients for the end-caps. As a first cross-check, and wherever it is relevant, these inputs are compared to the EM barrel ones. The outputs of the method, *i.e.* the predicted physics pulse shapes, the optimal filtering coefficients, the calibration bias and the noise reduction, are discussed in section 3.2.

3.1 Basics of the method and inputs for the end-caps

The amplitude and time of a cell response to a physics signal are computed using an optimal filtering (OF) technique [9]. In this method, maximum amplitude (A_{max}) and peak time deviation from the assumed time (Δt) are linear weighted sums of the n numerized samples S_i, in ADC units after pedestal subtraction :

$$A_{max} = \sum_{i=1}^{n} a_i S_i \ , \quad A_{max}\Delta t = \sum_{i=1}^{n} b_i S_i \tag{1}$$

The number n of considered samples is 5 or 25 in the following. The computation of the optimal filtering coefficients a_i and b_i is performed for 50 phases and for each gain to minimise the noise contribution. This requires the knowledge of the noise autocorrelation between all samples, extracted from pedestal runs, and of the output pulse shape and its derivative. The main difficulty lies in the prediction of the physics pulse shape. This can be done thanks to the calibration system [3], which sends a well-known exponential signal I^{cali} on the cold electronics plugged on the detector edge which then follows the same readout path as the physics one (Figure 1). The output physics pulse $g^{phys}(t)$ can be predicted from the calibration one by factorising the read out chain transfer function through the following time-domain convolutions [1] [4] :

$$g^{phys}(t) = g^{cali}(t) \times \mathcal{L}^{-1}\left[\frac{(1+s\tau_{cali})(st_{drift}-1+e^{-st_{drift}})}{st_{drift}(f_{step}+s\tau_{cali})}\right] \times \mathcal{L}^{-1}\left[\frac{1}{1+s^2LC+srC}\right] \tag{2}$$

where:

- $g^{cali}(t)$ is the cell response to the exponential calibration signal. This will be described in section 3.1.1.
- The first term in the Laplace domain takes into account the different input signal shapes between physics and calibration : exponential, with f_{step} and τ_{cali} as main parameters, for calibration and triangular, with t_{drift} slope time, for physics. They will be detailed in sections 3.1.2 and 3.1.3, respectively.
- The second term in the Laplace domain takes into account the different injection points between physics and calibration : the physics current is generated inside the detector and reaches the cold electronics through an inductive path, while the calibration pulse is injected on the mother board. This involves the electrical cell parameters r, L and C, introduced in section 2 and that will be discussed in section 3.1.4.

[3] An alternative method predicts the ionisation pulse from a complete description of the read-out cell [10].

[4] The attenuation by skin effect is not considered here as the calibration cable length is constant in the end-cap.

3.1.1 Cell response to a calibration signal

Typical shapes of cell responses to a same calibration input are shown in Figure 2 (left) for the three EMEC layers. The differences between shapes are explained by the electrical characteristics of each layer. Notice that, in the finely segmented part of the front sampling, $1.5 < \eta < 2.4$, the crosstalk between neighbour cells is important, between 3 and 5% [11], and has been taken into account by adding the two neighbouring cell shapes to the pulsed one. As a global sanity check, the dispersion along ϕ of the maximum amplitude of all calibration shapes is shown to be the same for all layers and exhibits no dependency as a function of η (Figure 2, right).

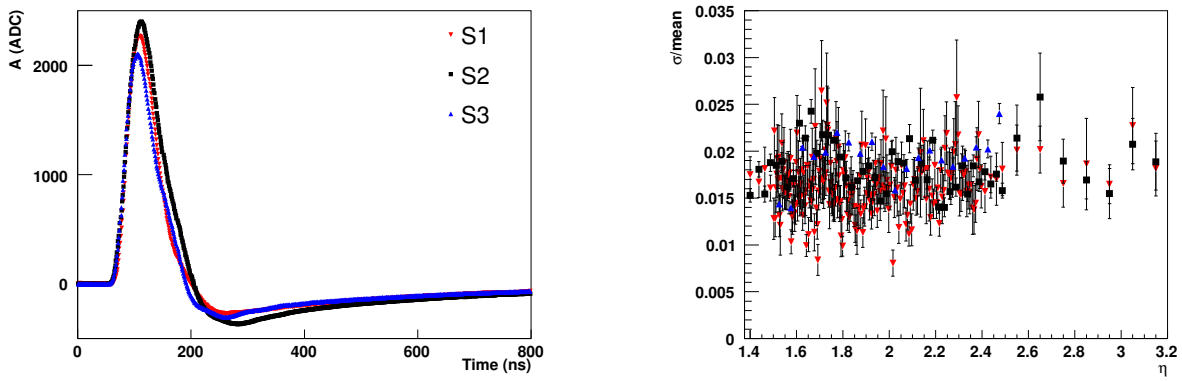

Figure 2: *Left: Typical calibration pulse shapes at* $\eta = 1.8$ *for an input of 500 DAC units in high gain. Right: Dispersion over* ϕ *of the maximum amplitude of all calibration shapes in high gain, as a function of* η*. Front, middle and back cells are represented with red down triangles, black squares and blue up triangles, respectively.*

3.1.2 Calibration board parameters

To obtain an efficient calibration, the input signal should be as similar as possible to the ionisation triangular pulse. Two main parameters, τ_{cali} and f_{step}, are needed to describe this calibration input pulse:

$$I_{inj}^{cali}(t) = I_0^{cali} \cdot \theta(t) \cdot \left[(1 - f_{step})e^{-\frac{t}{\tau_{cali}}} + f_{step}\right] \quad (3)$$

where $\theta(t)$ is the unit step function. The exponential decay time τ_{cali} is chosen to mimic the decay slope of the ionisation signal, while f_{step} is related to the resistive component of the inductance in the calibration board [1].

These two parameters need to be known for every calibration board channel. They can be extracted from measurements in the production laboratories [12] or can be inferred from the cell response to a calibration pulse using the Response Transformation Method (RTM) [1]. Figure 3 shows a comparison between the two methods for both parameters of one calibration board. Relative systematic shifts of -7% and $+15\%$ using RTM compared to the measured values are observed for extracted τ_{cali} and f_{step}, respectively, which is as expected in very good agreement with what was already reported for the barrel. This is probably because RTM gives effective parameters, absorbing for instance attenuation effects [13, 14]. As not all calibration

board measurements were available, the RTM extracted parameters are chosen to be consistent. Notice that choosing the RTM extracted parameters impacts only the absolute energy scale, which can not be tested very precisely with cosmic data.

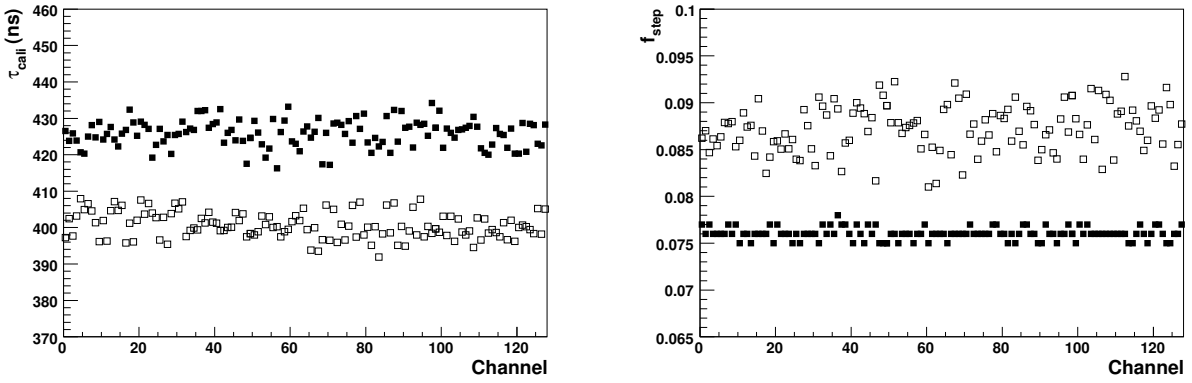

Figure 3: *Comparison of τ_{cali} (left) and f_{step} (right) extracted by RTM (open symbols) and measured directly (closed symbols) for the 128 channels of one calibration board.*

3.1.3 Ion drift time in liquid argon gap

The ion drift time in liquid argon gap, t_{drift}, can be expressed in terms of applied high voltage U and gap thickness g [15]:

$$t_{drift} = \frac{g}{V_{drift}} \sim \frac{g^{b+1}}{U^b} \tag{4}$$

where $b \sim 0.4$ is a parameter first determined with specific measurements [15] and then cross-checked with beam tests [16, 17, 18]. As indicated in section 2, the complicated EMEC geometry implies a variation of the gap thickness along η, which induces a varying drift time despite the change in the high voltage. This is a major difference with the barrel part, for which the drift time is almost constant around 470 ns for $U = 2000$ V.

The drift time can be computed using Equation (4) or extracted from a fit to the physic pulse shapes recorded with test-beam data [5] [17], with a precision estimated around 10%. Figure 4 shows the measured t_{drift}, averaged over ϕ, as a function of η for all EMEC layers [6]. They are in good agreement with the predictions extracted from Equation (4). Notice that any change on HV setting conditions implies a change of the drift time in the corresponding region.

3.1.4 Electronic chain characteristics

A thorough program of measurements was carried out at cold on all cells of the EMEC calorimeter before installation of the front end electronics to measure their electrical properties as precisely as possible. By means of a Network Analyser [12], a frequency scan was performed to

[5] At the beam tests, as events are asynchronous with respect to the clock, the 5 sample physics pulse in a cell can be averaged within a 1 ns bin by using the phase of each event.

[6] No measurement was available in the region $1.4 < |\eta| < 1.6$, in which the prediction is therefore taken.

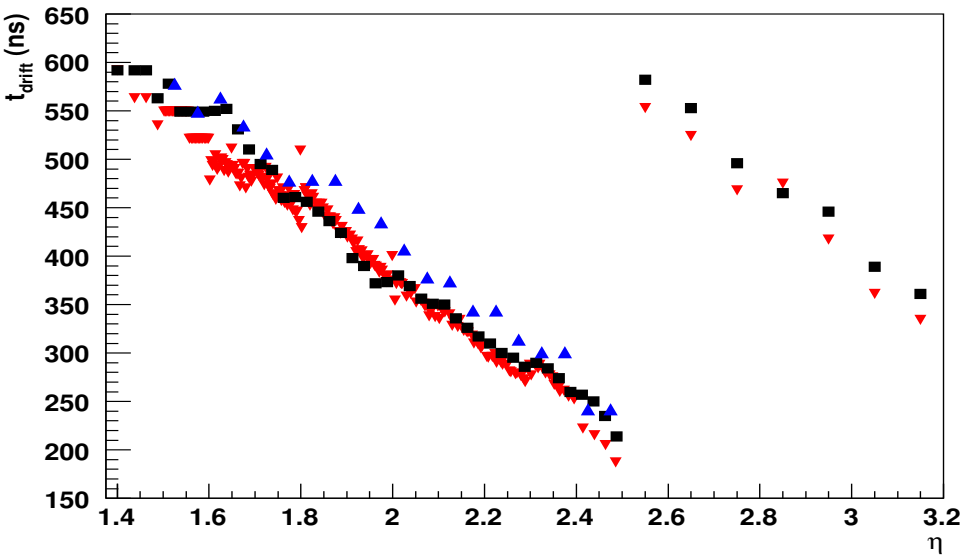

Figure 4: *Drift time as a function of* η *for front (red down triangles), middle (black squares) and back (blue up triangles) end-cap layers. All points have been averaged over* ϕ.

extract precisely the resonance frequency of the cell circuit $\omega_0 = 2\pi\nu_0 = 1/\tau_0 = 1/\sqrt{LC}$ and the product $\tau_r = rC$. In both cases, the most precise measurements were obtained in the second layer (first layer in the inner wheel), where capacitances are higher. Results are more difficult or impossible to extract in the first and third layers, and the approximation $\tau_0 = \tau_r = 0$ is therefore used in the following for these samplings.

Resonance frequency

Typical examples of end-cap S2 cell responses to a frequency scan with a Network Analyser are shown in Figure 5 (top). The resonance frequency is clearly visible on the left-hand plot, and is obtained by fitting a parabola around the minimum. The determination of the resonance frequency can be complicated by the presence of reflections near the peak, as illustrated in the second column of Figure 5 (top). This situation is even more pronounced when the resonance frequency is higher, *i.e.* the capacitance and the inductance are low, as for example at high η in the EMEC outer wheel (fourth column of Figure 5 top). In the last two cases, the resonance frequency is inferred by fitting the edges of the two minima with straight lines and computing the intercept point of both lines. To partly overcome this problem, ω_0 is not measured for every cells but averaged over ϕ at every η. Results are shown in Figure 6 (closed symbols). Their η-dependency, qualitatively reproduced by individual measurements of L and C [19], reflects the decrease of L and C as a function of η. This has to be compared to the barrel case, with a ω_0 varying only between 0.13 and 0.19 GHz [12].

Because of the uncertainties in the resonance frequency measurement described above, it is desirable to extract ω_0 with an alternative method, *i.e.* RTM in this case. The corresponding output functions [7] are illustrated for the same cells as for the measurements in Figure 5 (bottom). In all cases, comparable results with measurements are obtained, apart in the third column where the resonance frequency is 20% higher. Figure 6 shows RTM and measurement results

[7] The resonance frequency corresponds to the minimum of the function.

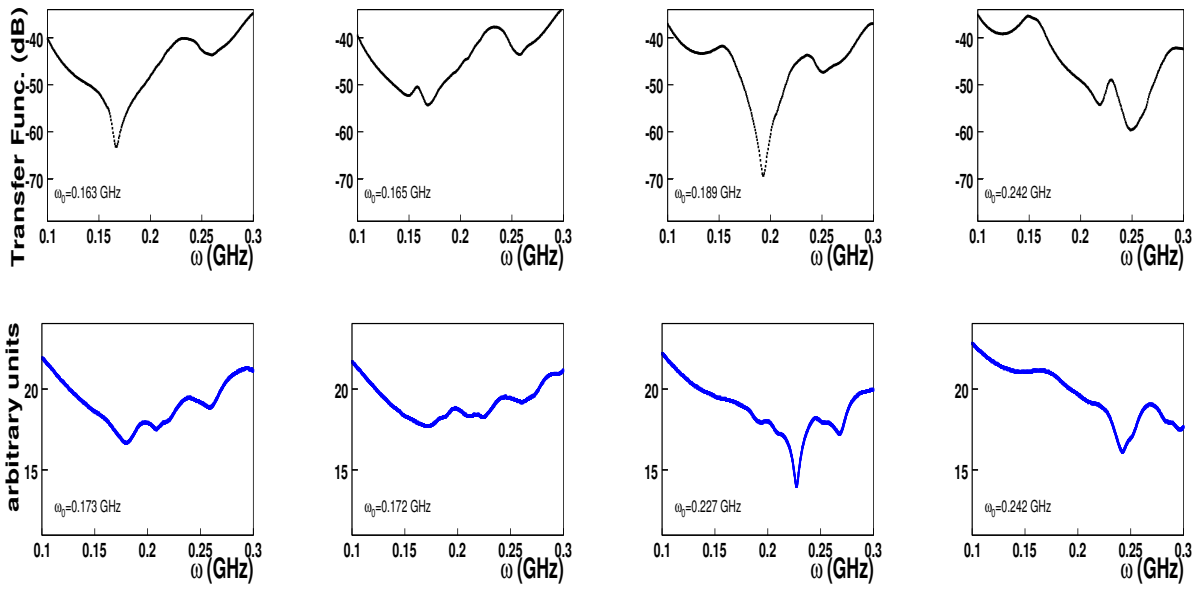

Figure 5: *Typical S2 cell responses in the 100-300 MHz frequency range at* $\eta = 1.6$ *(first row),* $\eta = 1.7$ *(second row),* $\eta = 1.8$ *(third row) and* $\eta = 2.2$ *(fourth row), as measured with a network analyser (top) and with the RTM method (bottom).*

as a function of η in S2. The agreement is good in the regions with high capacitances ($\eta < 1.7$ and $\eta > 2.5$), close to the barrel situation [8]. The situation worsens in the regions with lower capacitances, *i.e.* $1.7 < \eta < 2.5$, where the disagreement between RTM and measurements can reach up to 10-15%. To study the systematic effect on energy measurement linked to this disagreement, the two different ω_0 sets are considered in the following. Results are presented in details in section 4.2.3.

rC measurement

The product $\tau_r = rC$ can be determined by measuring r and C separately. The r values can be extracted from the frequency scan measurements by looking at the pulse amplitude at the resonance frequency [12], whereas C can be taken from direct measurements performed after EMEC module stacking [19]. Figure 7 shows the τ_r values obtained by this method as a function of η. As for the resonance frequency, it is desirable to compare these measurements with the values extracted by RTM : a large disagreement is obtained, with measurements lower than RTM values by a factor ~ 5 (Figure 7). This is because RTM gives effective parameters, *i.e.* absorb some additional effects not considered in the LAr readout model [20]. Similar observations are made in the barrel, with a factor between RTM and measurements of $\sim 2-3$ [21]. However, the impact on the amplitude determination is very small [1], and the measurements can not be used to predict the physics shapes, as it generates residual oscillations in the tails [20]. This is illustrated in Figure 8 in the end-cap case, and is similar for the barrel. As a consequence, RTM extracted values will be used in the following.

[8] The agreement between measurements and RTM extracted values at combined test-beam was $\sim 1\%$ for S2, well compatible with the precision required [4].

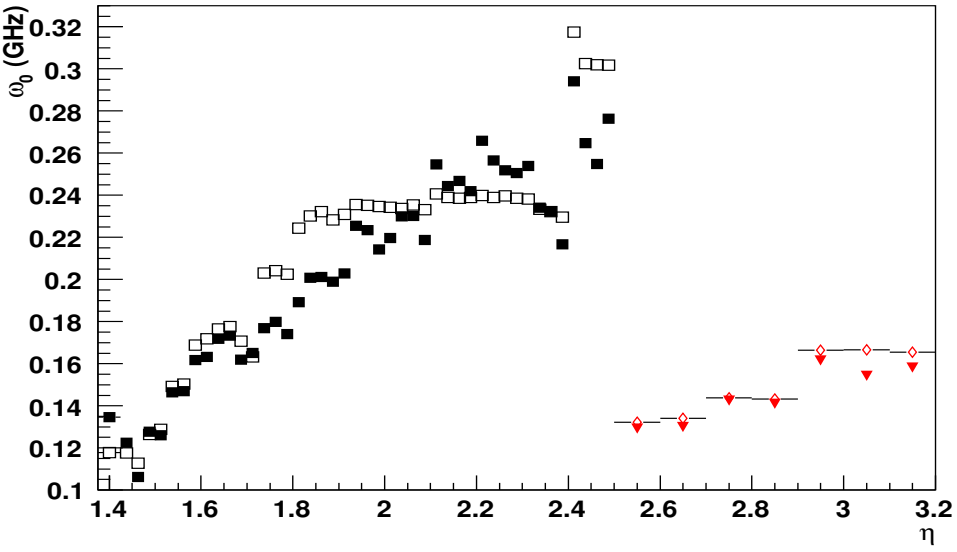

Figure 6: *Cell resonance frequency* ω_0 *obtained with network analyser measurements (closed symbols) and extracted with RTM (open symbols), as a function of* η *for S2 cells (S1 in inner wheel). All points have been averaged over* ϕ.

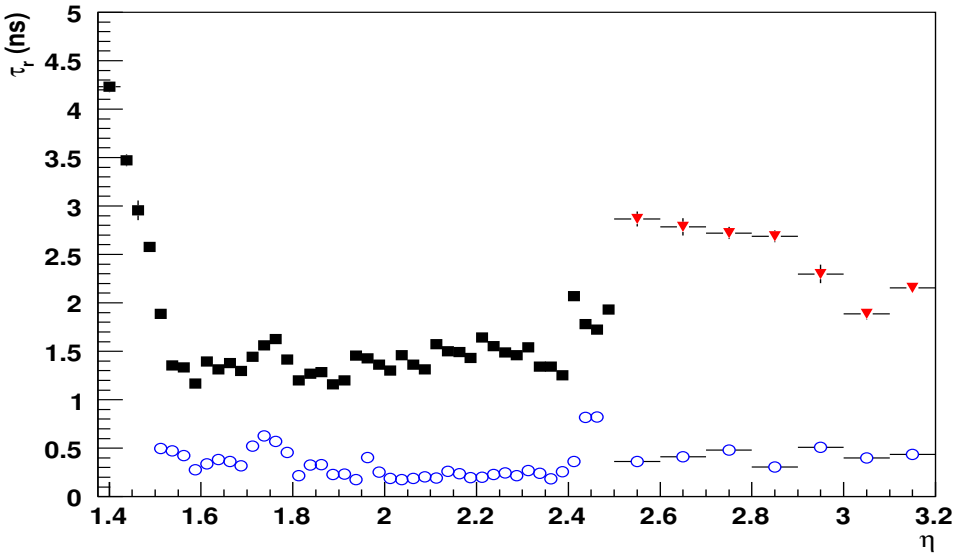

Figure 7: *Comparison of cell* τ_r *computed from the product of the measured r and C (open symbols) and extracted with RTM (closed symbols), as a function of* η *for S2 cells (S1 in inner wheel). All points have been averaged over* ϕ.

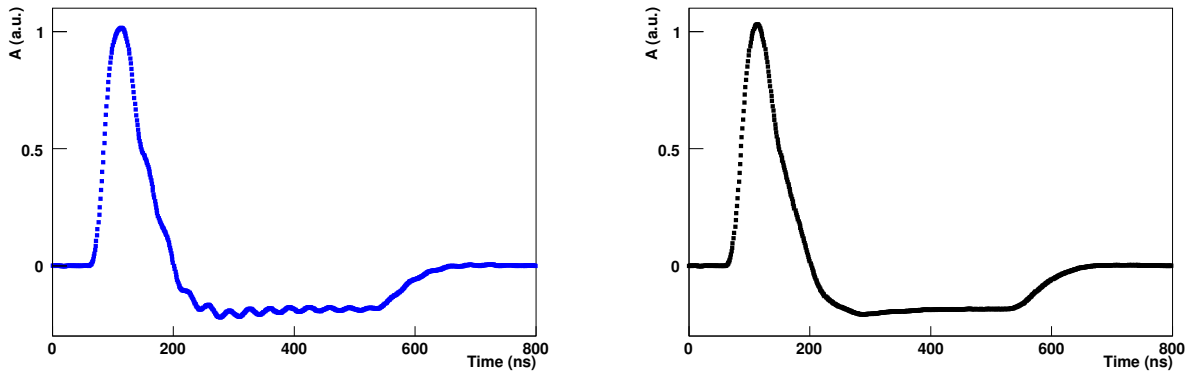

Figure 8: *Typical predicted physics pulse shape computed with measured τ_r (left) and RTM τ_r (right) at* $\eta = 1.8$.

3.1.5 Summary of the inputs

Except t_{drift}, all input parameters for signal reconstruction in the end-caps have been either directly measured or inferred from calibration system through RTM method. The choice made between both has been discussed in the previous sections. The situation is very similar to the barrel case for the calibration board parameters f_{step} and τ_{cali}, as well as for τ_r. It is different for ω_0 in the regions with a high resonance frequency ($1.7 < \eta < 2.5$), which renders the measurement difficult. To estimate the impact of a mismeasurement of this parameter, two sets of input parameters are considered, which can further serve to estimate the related systematic uncertainties on signal reconstruction (section 4.2.3). Table 2 summarises the origin of the input parameters used to predict the physics pulse shapes in the end-caps. The ω_0 set coming from direct measurements will serve as reference in the following, and therefore used unless otherwise stated.

	Outer Wheel			Inner Wheel	
Parameter	S1	S2	S3	S1	S2
f_{step}	RTM	RTM	RTM	RTM	RTM
τ_{cali}	RTM	RTM	RTM	RTM	RTM
t_{drift}	meas.	meas.	meas.	meas.	meas.
τ_r	0	RTM	0	RTM	0
ω_0 - Reference	0	meas.	0	meas.	0
ω_0 - Set 2	0	RTM	0	RTM	0

Table 2: *Origin of input parameters used for signal reconstruction in the end-caps. RTM refers to the Response Transformation Method [1], which infers the parameters from the cell response to a calibration pulse. Meas. refers to extensive measurements performed before the installation of the front end electronics. The two* ω_0 *sets will be used to compute the two sets of optimal filtering coefficients later tested in the cosmic muon run analysis (section 4).*

3.2 Outputs of the method

3.2.1 Computation of the pulse shapes and optimal filtering coefficients for physics

All input parameters discussed in section 3.1 enter directly in Equation (2) to predict the physics pulse shape of each EMEC cell. Typical shapes can be seen in Figure 9 (left) for the three EMEC layers. As a first check on the quality of this prediction, the dispersion along ϕ of the maximum amplitude is shown as a function of η for the three layers in Figure 9 (right). It is roughly constant below 0.1% for S1 and S3 in the precision region ($1.5 < |\eta| < 2.5$). It decreases with η in S2, following the τ_0 variation [9]. Notice that the same results are obtained with the two ω_0 input sets of Table 2. More quantitative checks of the quality of these predicted shapes are proposed in section 4.2.2 using cosmic data.

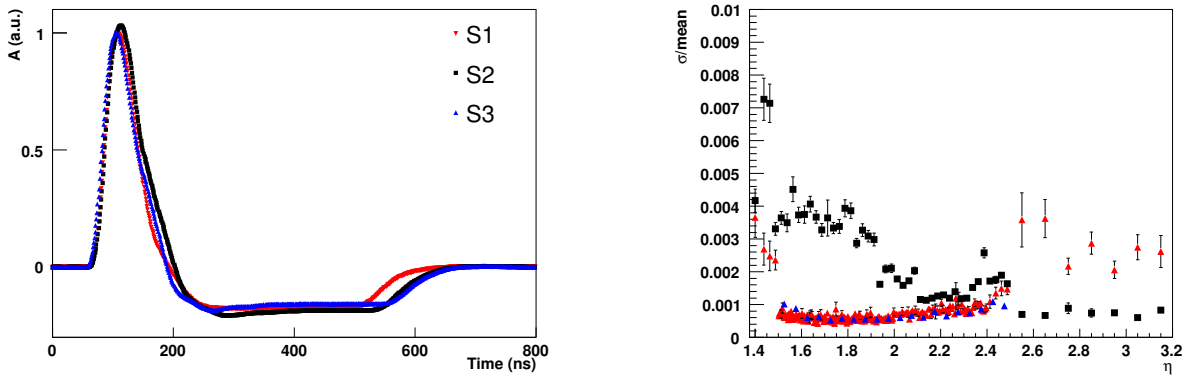

Figure 9: *Left: Typical predicted physics shape at* $\eta = 1.8$ *in high gain. Right: Dispersion over* ϕ *of the maximum amplitude of all physics shapes in high gain, as a function of* η*. Front, middle and back cells are represented with red down triangles, black squares and blue up triangles.*

From these physics pulse shapes and their derivatives, optimal filtering coefficients (OFC) a_i and b_i are computed per cell for each gain and for 50 phases by 1 ns step. This has been done with 5 or 25 samples and using one of the two input parameter sets of Table 2. Unless otherwise stated, the case with 5 samples and reference input set is used in the following.

3.2.2 Estimation of the calibration bias

The difference between physics and calibration shapes induces a different response amplitude to a normalised input signal. The resulting bias must be taken into account in order to correctly convert ADC counts into energy. This is achieved by using the ratio between the maximum amplitudes of physics and calibration pulses, called $\frac{M_{phys}}{M_{cali}}$. It is shown in Figure 10 as a function of η for the 3 EMEC layers in high gain [10]. The decreasing behaviour with η reflects at first order the cell inductance variation [19] (mainly visible for S2), and at second order the drift time variation (visible for S1 and S3 where the inductance is assumed to be zero, $\tau_0 = \tau_r = 0$).

[9] It was checked that using $\tau_0 = \tau_r = 0$ in S2, results become similar to S1 and S3.

[10] It was checked that the gain has no impact on the ratio.

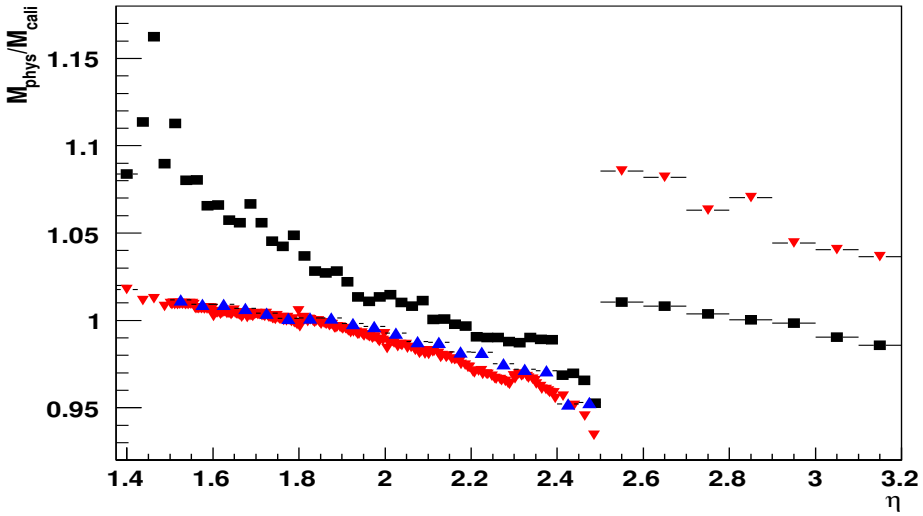

Figure 10: *Bias in the signal reconstruction method* $\frac{M_{phys}}{M_{cali}}$ *in front (red down triangles), middle (black squares) and back (blue up triangles) EMEC cells. All points have been averaged over* ϕ*. High gain and the reference input set of Table 2 are used.*

A comparison with $\frac{M_{phys}}{M_{cali}}$ values obtained with 2001-2002 test beam analysis [3] is proposed in Figure 11 (left). The differences are quite important, at the level of $5-8\%$ in the region $1.5 < \eta < 2.4$, reflecting the different conditions of both analyses and data takings : cable lengths, optimal filtering coefficient computations, calibration and front-end electronics, etc. As a systematic check, it is interesting to make the same comparison between the two ω_0 input sets of Table 2. The agreement is at the percent level, as shown in Figure 11 (right). Finally, notice that the prediction of this bias on the signal reconstruction method can hardly be checked with commissioning data, since the absolute muon energy scale is only known at $\sim 5\%$ [5]. The uncertainties on $\frac{M_{phys}}{M_{cali}}$ ratio will later be absorbed in the inter-calibration coefficients extracted with electrons from Z decay [22].

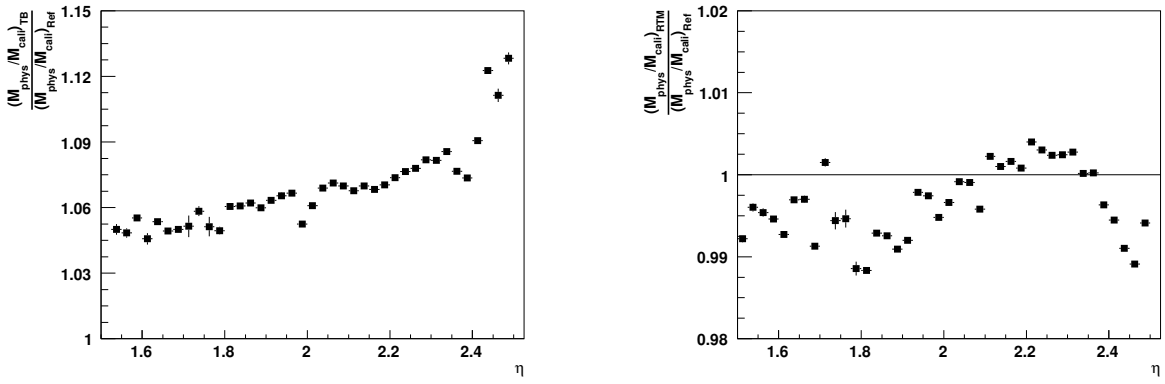

Figure 11: *Ratios of* $\frac{M_{phys}}{M_{cali}}$ *in S2 between the present analysis with the reference set and 2001-2002 test beam analysis [17] (left) and between the two* ω_0 *input sets of Table 2 (right).*

3.2.3 Noise reduction with optimal filtering technique

The computation of the optimal filtering coefficients (OFC) is performed to minimise the noise contribution to the signal reconstruction. To check this noise reduction, the OFC are applied to pedestal runs for different number of samples. The noise level obtained using 5 samples in high gain, averaged over ϕ, is shown in Figure 12 for the three EMEC layers as a function of η. In the precision region $1.5 < \eta < 2.5$, weak variations are observed along η and average noise values of 14, 32 and 27 MeV are measured for the three samplings, respectively. This agrees nicely with the module test-beam results [16].

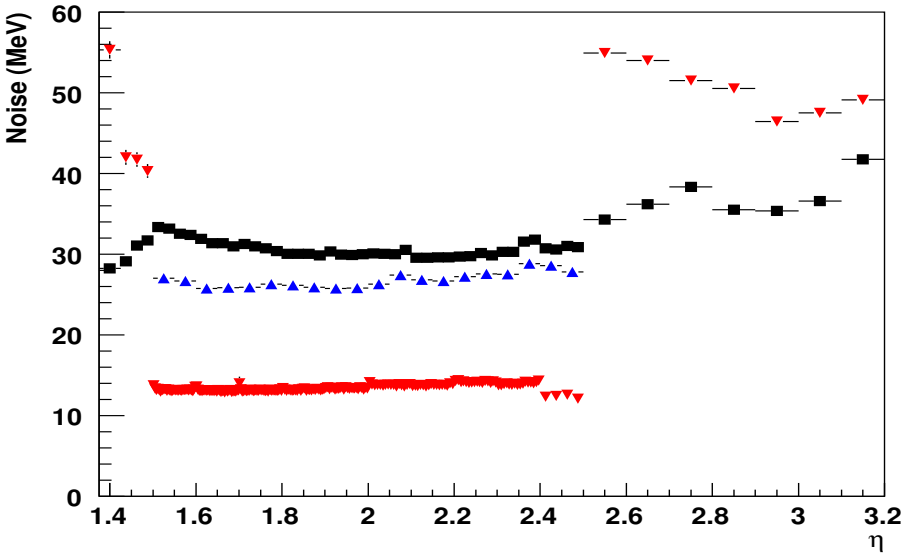

Figure 12: *Total noise computed with 5 samples OFC in high gain, averaged over* ϕ *and as a function of* η*, for front (red down triangles), middle (black squares) and back (blue up triangles) EMEC cells.*

The noise reduction obtained with optimal filtering technique increases with the number of samples used, as more signal information is available and the noise correlation between samples is better accounted for. This is illustrated in Figure 13 at $\eta = 1.8$ for the three layers. Reduction factors of 1.5 (1.4) and 2.4 (2.2) are obtained in the second (first) layer using 25 samples compared to 5 and 1, respectively. These results are slightly lower than those obtained in the barrel, $\sim$1.8 (1.8) and $\sim$2.9 (2.6) [5] because of lower capacitances in the end-cap. Figure 14 shows the noise reduction in S2 as a function of η using 5 (left) and 25 (right) samples with respect to one single sample. Smooth behaviours are observed in the regions $1.5 < \eta < 2.5$ and $2.5 < \eta < 3.2$. The more pronounced variation for 25 samples is at first order a consequence of the drift time variation (Figure 4) : a lower drift time gives a shorter waveform. As a consequence, the number of meaningful samples decreases with η, degrading the reduction factor brought by the optimal filtering technique.

It is interesting to notice that these results on noise can serve as a benchmark to check the computation of the physics OFC, and can also point to a wrong latency setting of the read-out [23]. They therefore give confidence on the quality of the data taking set-up and of the autocorrelation matrix and OFC computation. This allows to go further, and perform an analysis of the small signals deposited by cosmic muons over the complete calorimeter coverage, $0 < \eta < 3.2$. This is the subject of the next section.

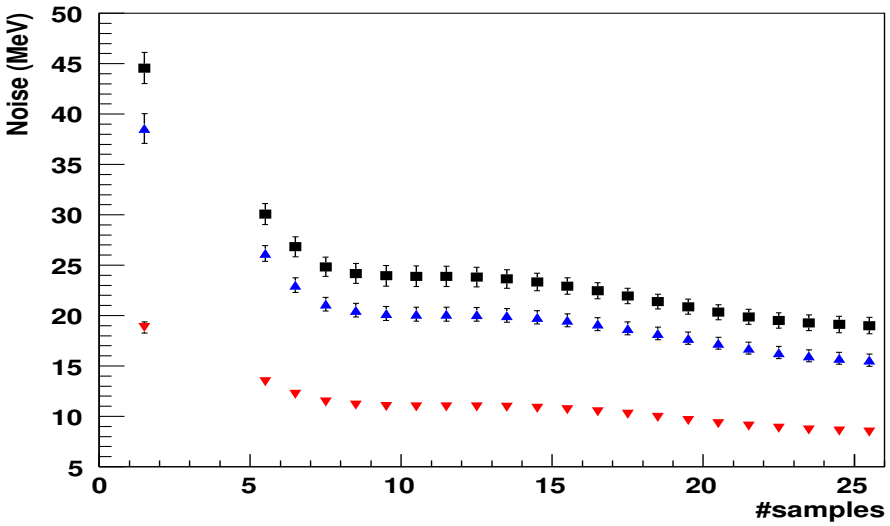

Figure 13: *Noise as a function of the number of samples used by optimal filtering for the three EMEC layers in high gain at* $\eta = 1.8$. *Front, middle and back cells are represented with red down triangles, black squares and blue up triangles.*

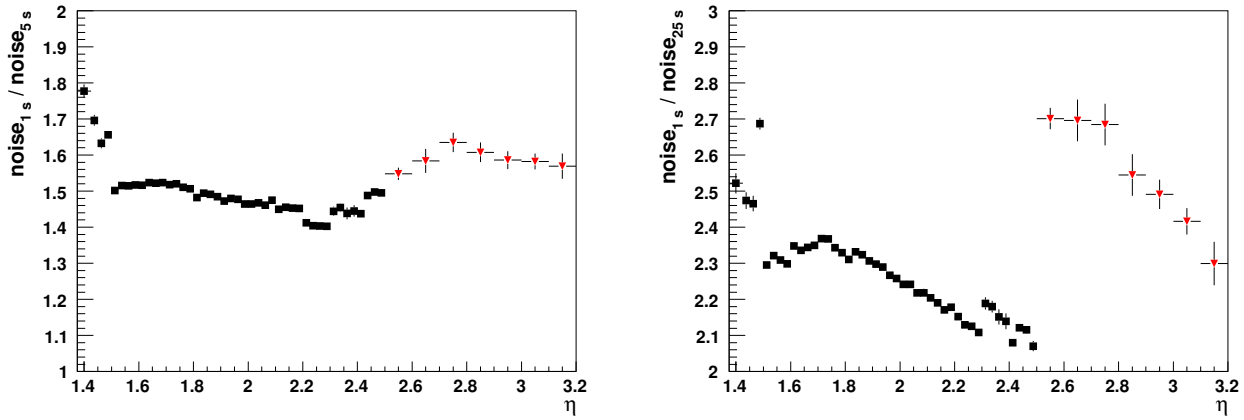

Figure 14: *Noise reduction as a function of* η *in S2 (resp. S1) of the outer (resp. inner) wheel using 5 samples (left) and 25 samples (right) OFC, compared to one single sample.*

4 Checking signal reconstruction in $|\eta| < 3.2$ with cosmic data

The first cosmic muon data were registered in the ATLAS cavern in August 2006 by the EM barrel calorimeter, in the regions equipped with front-end electronics. First studies focused on these regions (6% of the barrel) and concentrated on projective muon samples [5]. Since March 2007, one end-cap wheel [11] and the whole barrel are fully operational and take data regularly. Focusing on some dedicated cosmic muon runs (taken during "muon" weeks called M3 and M4 afterwards), it is therefore possible to perform a first study on the almost complete calorimeter coverage $-1.4 < \eta < 3.2$. This is particularly suitable to perform an *in situ* test of the signal reconstruction presented in section 3. Even with the limited available statistics ($\sim 150\,000$ triggered events), the selection of the few % of events with catastrophic high energy deposits (section 4.1) represents a good opportunity to check the signal reconstruction quality in a coherent way for both barrel and end-cap parts (section 4.2).

4.1 Selection of high energy deposits

Selecting projective muons imposes by default a barrel-restricted analysis. However, considering only events where a hard enough bremsstrahlung photon deposits its energy in the EM calorimeter can allow to perform an analysis in the complete coverage $|\eta| < 3.2$: in this case, the photon induces an electromagnetic shower, detected more easily and independently of the incident muon projectivity. Moreover, this selects "electron-like" energies, of the order of the GeV, which are well suited to test the signal reconstruction procedure.

4.1.1 Conditions of data taking

Since the ATLAS muon trigger was not available on the full coverage (especially in the end-caps) at the time of data taking, a dedicated trigger, using only Tile calorimeter signals, was configured to detect cosmic muons. The available Tile towers, $\Delta\eta \times \Delta\phi = 0.1 \times 0.1$, were asked for a top-bottom coincidence [24] to form the trigger for each data taking period, as shown in Figure 15. The compromise between noise and a too low trigger rate results in a ~ 1 GeV threshold per tower and a $\sim 50\%$ muon purity of the triggered events [5].

The main concern in the present analysis is related to the available statistics. This issue is strongly correlated with the trigger set-up. Therefore, even if data are taken nearly every week-end over the whole calorimeter since spring 2007, only runs with stable enough data taking conditions are selected for this analysis (Table 3). All data were collected in high gain and $\sim 150\,000$ triggered events are available. It should be noticed that, contrarily to the end-caps, the barrel did not operate under nominal HV but used a reduced value of 1600 V to be better protected from unstable conditions in the cavern. As a consequence, the optimal filtering coefficients were recomputed and the factor converting ADC to MeV was divided by 0.919 [5].

[11] the $z > 0$ side, called ECA wheel. The other side, called ECC wheel, can be integrated in the analyses since M5 period, *i.e.* beginning of November.

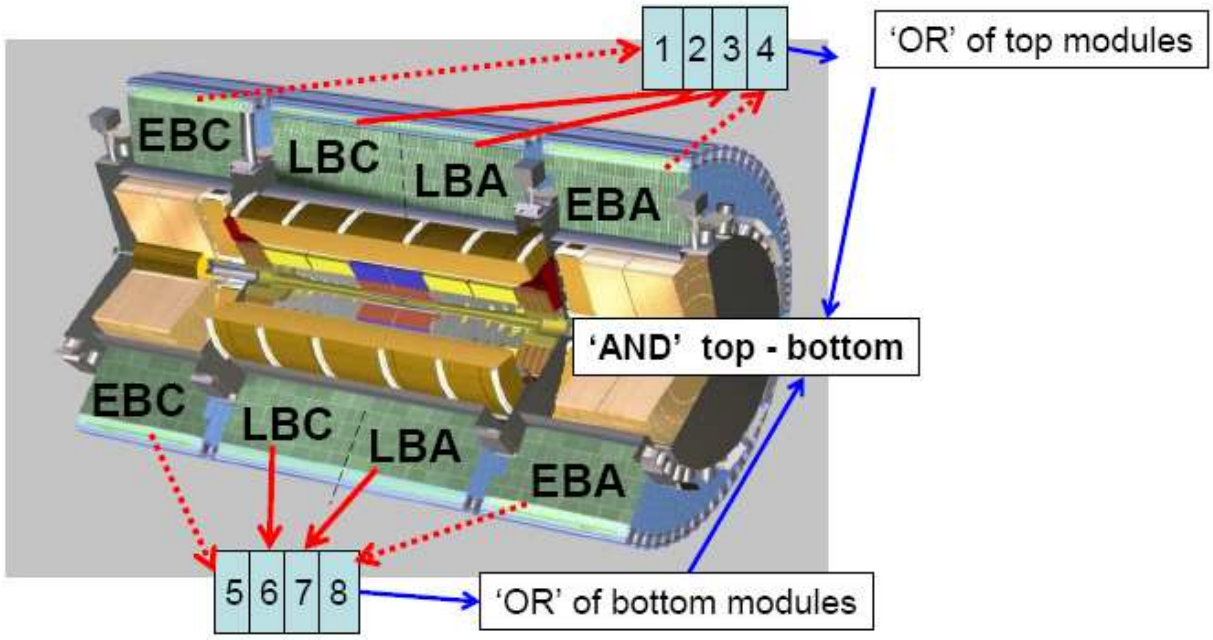

Figure 15: *Tile trigger setup and logic of the top-bottom coincidence. The extended barrel part EBC was not available for the runs analysed in this note.*

Date in 2007	# of runs (Run #)	Tile Trigger (Figure 15)	Triggered Evts ($\times 10^3$)	# of cells with E> 500 MeV (analysed evts)	
				Barrel	End-cap
29/06-07/07	5 (14066→14848)	EBA	11.2	0 (0%)	490 (100%)
06/09-09/09	6 (23381→24609)	LBA, LBC, EBA	71.4	1276 (52%)	593 (100%)
14/09-16/09	6 (24847→24874)	LBA, LBC, EBA	66.3	1775 (42%)	373 (68%)
Total	17	–	148.9	3051 (44%)	1456 (86%)

Table 3: *Characteristics of cosmic runs used in the analysis: run #, trigger set-up, statistics and number of cells with E> 500 MeV (see text for more details). For technical reasons (castor access) and lower statistical limitations, only half of the statistics has been analysed for the barrel, whereas almost the complete statistics has been analysed for the end-cap.*

4.1.2 Selection criteria

Unless stated otherwise, the energy is reconstructed with optimal filtering technique using 5 samples [12]. The conversion factor from ADC counts to MeV, presented in Figure 16, is computed by factorising the cell gain, $\frac{M_{phys}}{M_{cali}}$, the injected current from the calibration and the sampling fraction. A good agreement is obtained with the foreseen values [25].

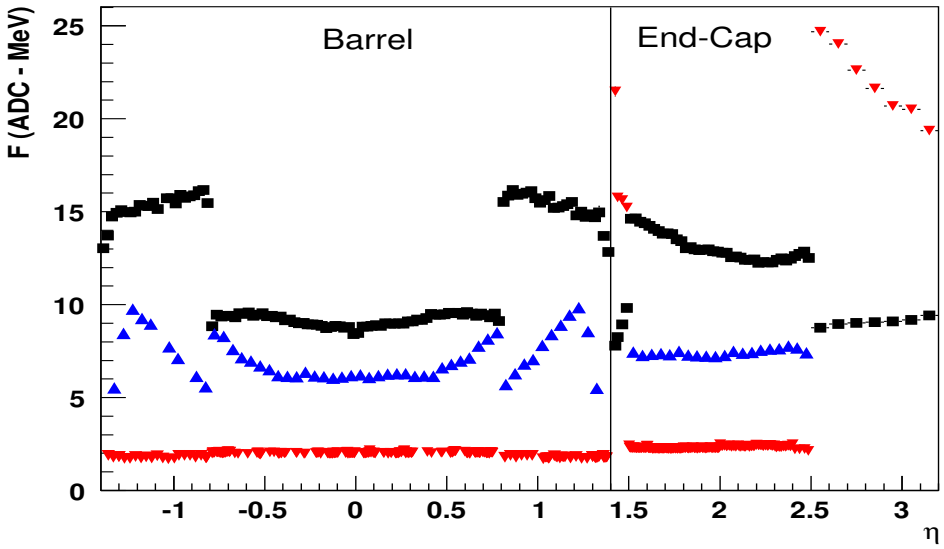

Figure 16: *ADC to MeV conversion factor (MeV/ADC) as a function of* η *for front (red down triangles), middle (black squares) and back (blue up triangles) cells. All points have been averaged over* ϕ*. High gain and the reference input set of Table 2 are used.*

To minimise the fluctuations in the signal reconstruction, the energy deposited per cell should be well above the noise. On the contrary, for statistical reasons, the present analysis can not be performed if the threshold on the energy is too high, and a good compromise is found by requiring $E > 500$ MeV. At this stage, the OFC phase of each cell should be known, *i.e.* the iterative process to determine Δt in Equation (1) should have converged ($|\Delta t| < 1$ns). Thanks to the "high" energy cut, more than 99% of the cells fulfill this condition. Failing cases are mainly due to a badly adjusted latency (maximum of the pulse in the first sample).

One of the main difficulty of this analysis is to reject the cells wrongly selected with high energy, due to high noise or incorrect pedestal subtraction. A simple and robust criterion to tag these fake cells is to impose that a given cell is selected only once per run, reflecting the very low probability that randomly produced bremsstrahlung photons deposit their energy in the same cell twice per run. As only high gain is available, cells with more than 2500 ADC counts [13] after pedestal subtraction are also rejected to avoid saturation effects. After this selection, $\sim$1500 cells are selected in the end-cap and $\sim$3000 in the barrel (Table 3).

[12] The same calibration constants (pedestal, autocorrelation matrix, ramp) are used for all runs.

[13] This corresponds roughly to 6 GeV in S1, 35 GeV in S2 and 17 GeV in S3.

4.1.3 Map of selected cells

The mapping of the selected cells is presented in Figure 17 in the front-end electronic boards (FEB) coordinates, and Figure 18 in the $\eta - \phi$ plane for each layer. In both barrel and end-cap, the statistics is almost equally spread in each FEB slot corresponding to the second layer [14]. The increase in top and bottom regions [15], due to the down-going cosmic direction, is clearly visible.

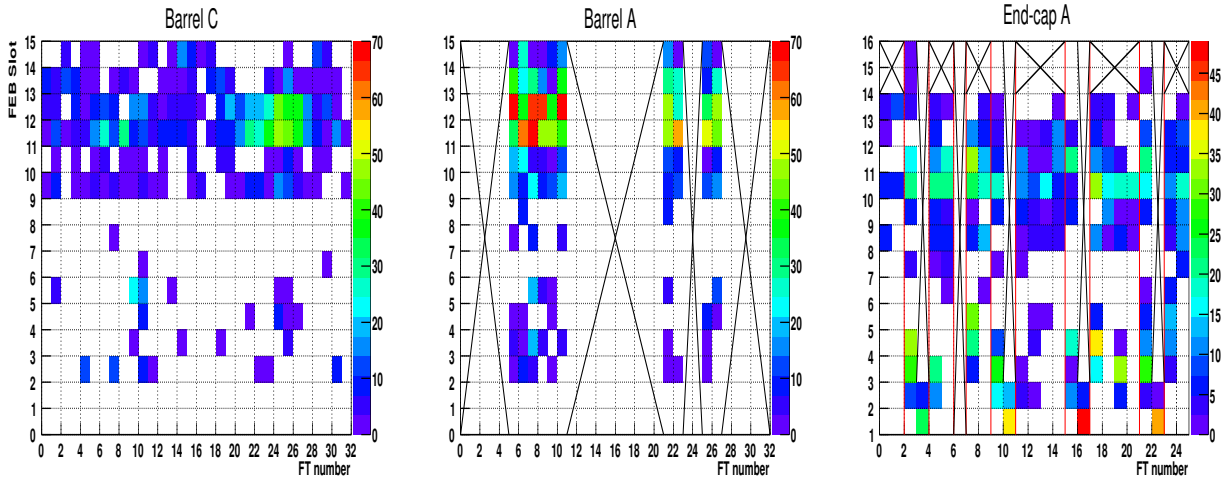

Figure 17: *FEB slot - feedthrough (FT) number mapping of high energetic cells in the barrel C (left), barrel A (middle) and end-cap A (right). Crosses indicate the unplugged electronics in the barrel and empty slots or HEC/FCAL slots in the end-cap.*

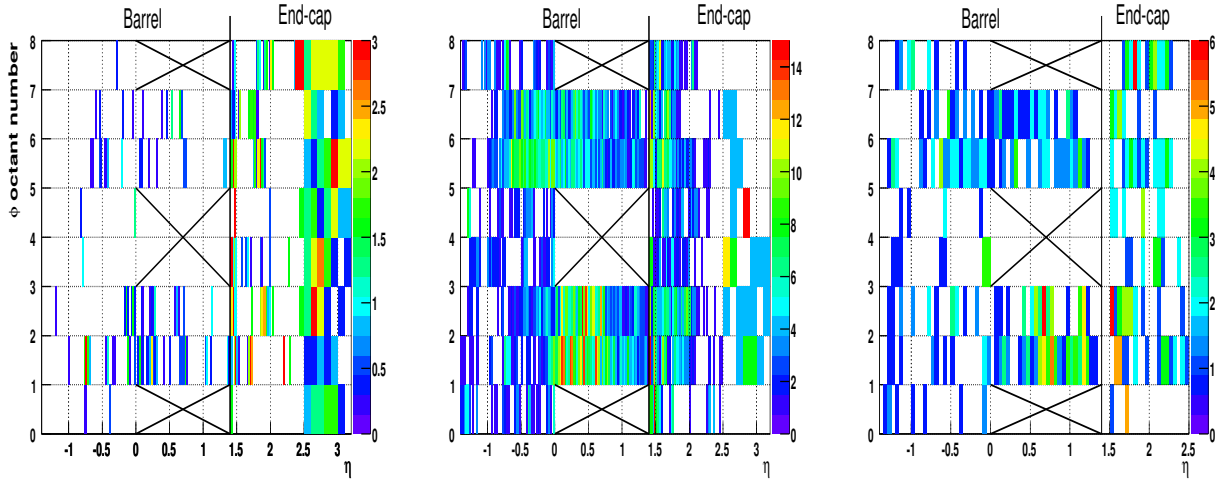

Figure 18: $\eta - \phi$ *map of high energetic cells in S1 (left), S2 (middle) and S3 (right) for* $-1.4 < \eta < 3.2$. *Crosses indicate the unplugged electronics in the barrel and empty slots or HEC/FCAL slots in the end-cap.*

[14] FEB slot $\geq 11(10)$ in the barrel (standard end-cap) crates. In special (HEC) crate FT 2, 9, 15, 21 (3, 10, 16, 22) it corresponds to slot number 3, 4, 10, 11, 14, 15 (2).

[15] FT 5-10 (4-8) and 21-26 (17-20) for top and bottom in the barrel (end-cap).

The energy distribution of the selected cells is shown in Figure 19 for the three layers of the barrel (left) and the end-cap (right). In the barrel, 80% of the statistics is concentrated in S2, the rest being shared between S1 and S3. In the end-cap, S2 cells represent only $2/3^{rd}$ of the statistics, because of the non-projective situation (the photons see the cell size in the $\eta - \phi$ plane and not the cell depth). The average energies of all distributions are around 1.5 GeV. It can be noticed that, given the small η size of S1 cells, the selection generally involves a group of cells per event, rather than isolated cells like in S2 or S3, as seen in Figure 18. This is illustrated in Figure 20, where a high energy shower (E$>$ 200 GeV) illuminates more than 50 S1 cells at $\eta \sim 1.8$.

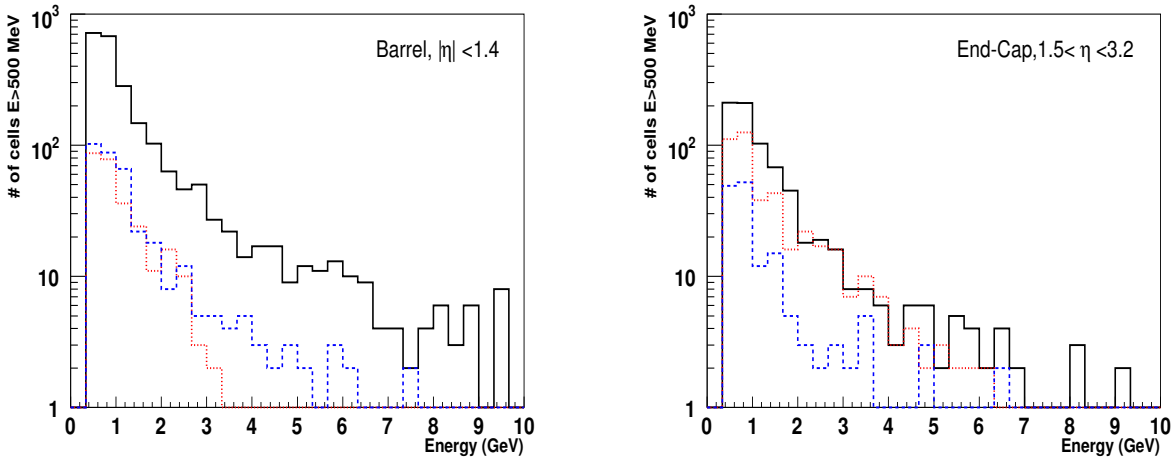

Figure 19: *Energy distribution of selected cells in the barrel (left) and in the end-cap (right). S1, S2 and S3 cells are represented with red dotted, black full and blue dashed histograms.*

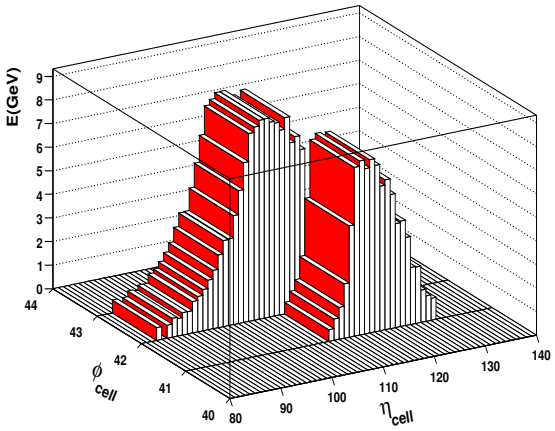

Figure 20: η-ϕ *mapping of a high energy shower (>200 GeV) in S1 at* $\eta \sim 1.8$. *In this event, 56 cells are above 500 MeV and 18 above the saturation threshold (∼6 GeV).*

4.2 Comparison of predicted physics pulse shapes with data

This section presents a check of the signal reconstruction performed over the full calorimeter coverage with cosmic data. The method is first explained, and the pulse shape predictions are then systematically and quantitatively compared to the cosmic data. Finally, the impact in the end-cap of resonance frequency and drift time uncertainties on the energy reconstruction is assessed.

4.2.1 Method to superimpose predictions and data

To compare the predicted physics pulse shapes (normalised to one) with the data for all selected cells, the first step is to multiply the prediction by the maximum amplitude computed with optimal filtering. Because of different FEB timings and asynchronous muon arrival times, a global time shift is then determined for each cell by minimising the following χ^2 through an iteration by steps of 25 ns :

$$\chi^2 = \sum_{i=1}^{n} \left(\frac{A_i^{data} - A_{max} * g_i^{phys}}{\sigma_{noise}} \right)^2 \tag{5}$$

where n is the number of samples considered, A_i^{data} is the amplitude of each sample i in ADC counts for data, A_{max} is the maximum amplitude defined in Equation (1) and g_i^{phys} is the predicted physics pulse shape defined in Equation (2). Finally, σ_{noise} corresponds to the noise for a single sample in ADC counts [16].

After this time adjustment, data and predictions can be compared. Figure 21 shows typical physics shapes for each sampling (S1, S2 and S3 from top to bottom) in the barrel (left) and in the end-cap (right). For 5 sample pulse shapes, the predictions agree nicely with the data in the raising and falling edges of the pulses. More quantitative conclusions are drawn in section 4.2.2.

For 25 samples, apart from the systematic bias observed around the maximum, a fair agreement is visible in the falling edge and in the undershoot, except for the highest sample numbers, which was already reported in [5]. A more quantitative discussion on these points is proposed in section 4.2.4.

[16] Approximately, 9/3/6 ADC counts in S1/S2/S3 for $|\eta| < 2.5$ and 6/5 ADC counts in S1/S2 for $|\eta| > 2.5$.

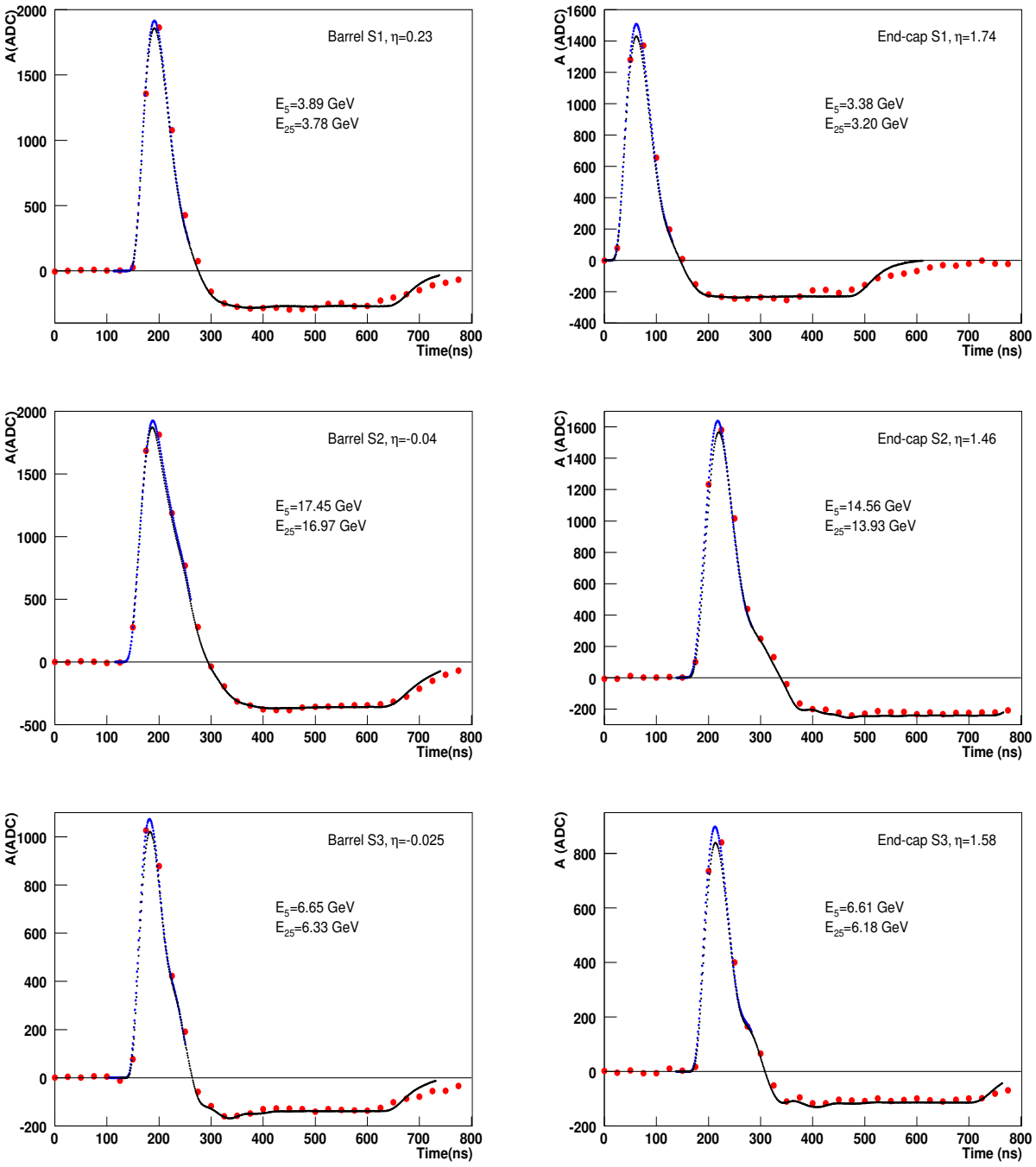

Figure 21: *Typical cell responses in high gain to high energy deposits in the barrel (left) and end-cap (right) layers (S1, S2 and S3 from top to bottom). The blue (resp. black) curves correspond to the predicted pulse shapes using 5 (resp. 25) samples.*

4.2.2 Quality of the predicted pulse shapes

The χ^2 proposed in Equation (5) can be used to perform a systematic quantitative comparison between data and pulse shape predictions over the full η coverage. By construction, this estimator of the prediction quality depends on the square of the energy. To allow a comparison between barrel and end-cap, whose energy spectra per layer are different (Figure 19), it is divided by the square of the reconstructed amplitude, ${A_{max}}^2$. Moreover, only 5 samples ($n = 5$) are considered, as this is what will be used to reconstruct the energy in ATLAS. The comparison with 25 samples will be presented in section 4.2.4.

Results for this estimator of the data/prediction comparison, $\chi^2/{A_{max}}^2$, are shown in Figure 22 as a function of the energy for the three layers (S1, S2 and S3 from top to bottom) in the barrel (left) and in the end-cap (right). It is fitted by the following simple function, which allows a very good modelling in all layers of the barrel and end-cap parts :

$$\frac{\chi^2}{n_{samples} \times {A_{max}}^2} = \frac{p_0}{E^2} + p_1 \tag{6}$$

The first term, dominating at low energy, is due to the gaussian noise fluctuation for each sample. It is hardly visible in S1, as the noise in this sampling is lower and already negligible for a 500 MeV energy deposit. The second term, dominating at high energy where the noise contribution can be neglected, reflects the quality of the predicted shape as compared with the data. The results are only slightly better in the barrel compared to the end-cap. This is the first proof of the quality of an ATLAS-like signal reconstruction in the end-caps, despite its challenging aspect. This is also illustrated in Figure 23, which shows the pulse shape prediction quality $\chi^2/{A_{max}}^2$ as a function of η between 0 and 3.2 for the three samplings [17]. These results are obtained by applying a lower energy cut (0.5, 1.5 and 1.2 GeV in S1, S2 and S3 respectively), to minimise the noise contribution, and an upper cut (2500 ADC counts) to avoid high gain saturation. Again, a smooth behaviour is obtained for both barrel and end-cap, with a slight worsening in the end-cap (mainly in S3). These results assess the coherence of the signal reconstruction quality, using 5 samples as foreseen in ATLAS, over the complete calorimeter coverage $0 < \eta < 3.2$.

It is finally worth mentioning that the computation of the χ^2 proposed in Equation (5) will be performed *on-line* above a given energy threshold in the Read-Out Driver modules [26], to control the quality of the signal reconstruction in all cells. This will be useful to mask the most problematic channels, as it was done in this analysis : a few cells exhibiting a too large χ^2 have been removed from Figures 22 and 23. The reasons leading to these bad physics shape data will be investigated.

[17] The absolute values of the quality estimator depend on the injection resistors, which are different between samplings.

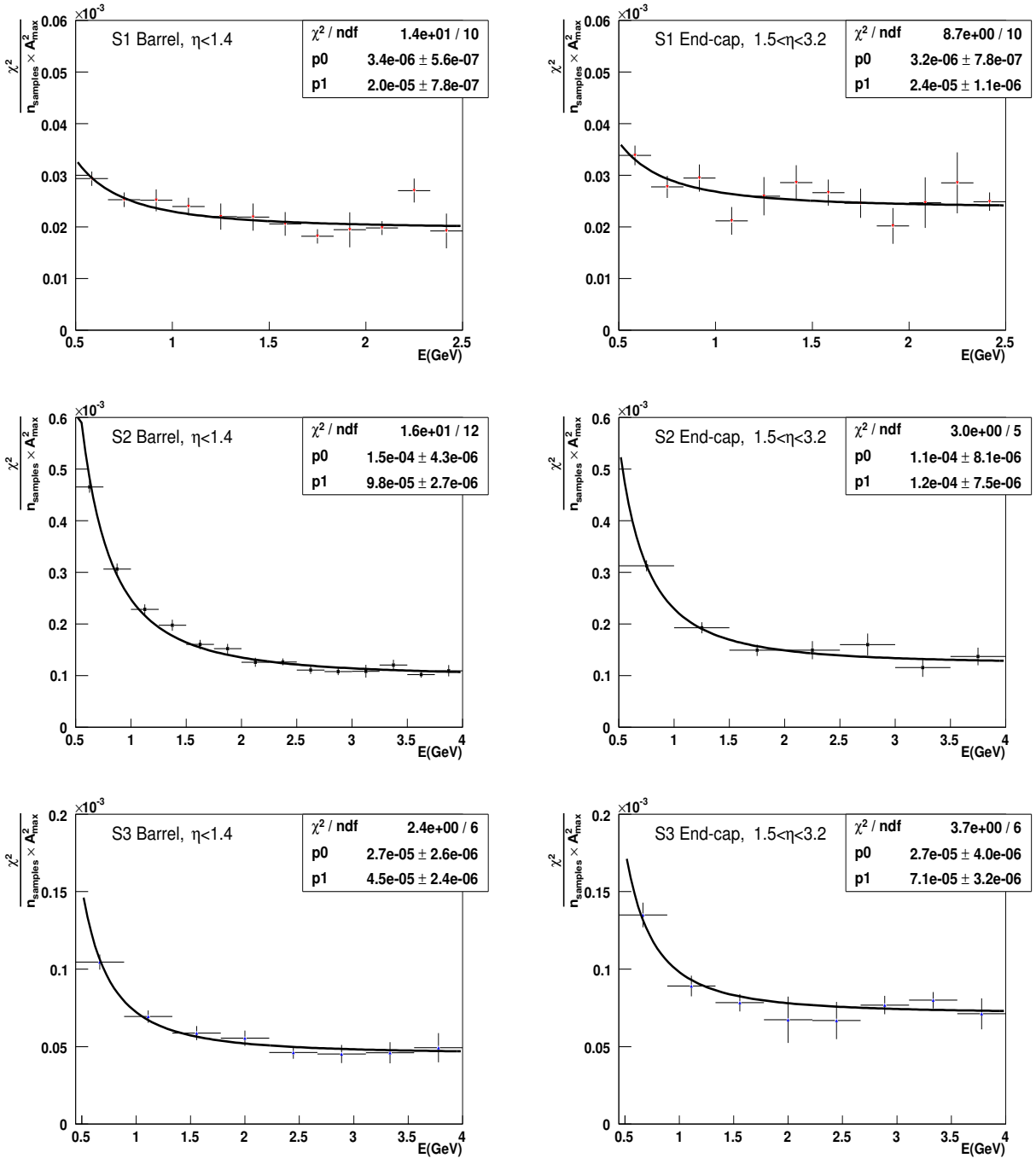

Figure 22: *Estimator $\chi^2/A_{max}{}^2$ of the quality of the predicted physics pulse shape as a function of the energy for the barrel (left) and the end-cap (right) in S1, S2 and S3 (top to bottom). 5 samples and high gain are used. The function used for the fit corresponds to Equation (6).*

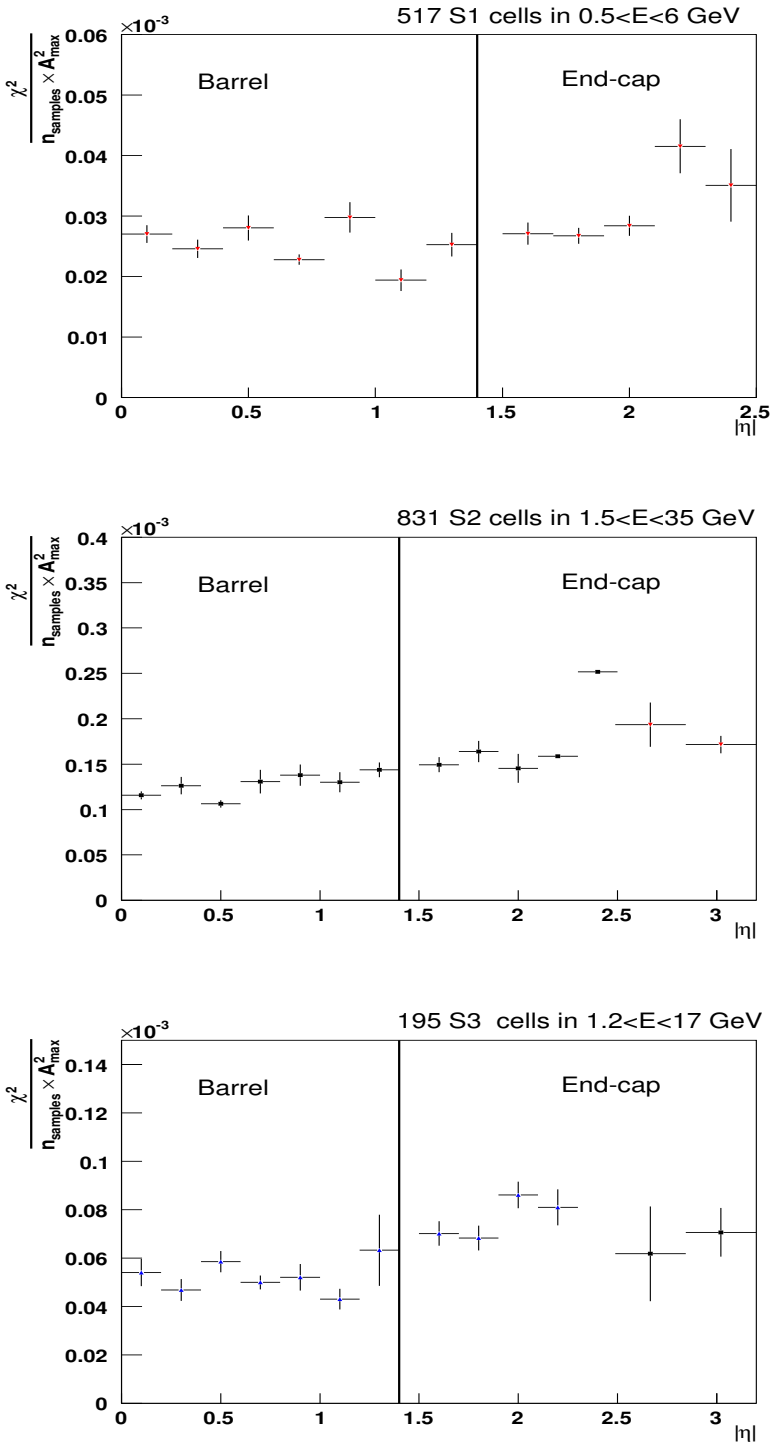

Figure 23: *Estimator* $\chi^2/A_{max}{}^2$ *of the quality of the predicted physics pulse shape as a function of* $|\eta|$ *for S1 (top), S2 (middle) and S3 (bottom). 5 samples and high gain are used.*

4.2.3 Main systematic uncertainty in the end-cap signal reconstruction

The main uncertainty from the input parameters concerns the resonance frequency values ω_0, for which the disagreement between different measurement methods can reach up to 10-15% (section 3.1.4). To estimate quantitatively the impact of this uncertainty on the energy reconstruction, two sets of optimal filtering coefficients have been built (reference set and set 2 of Table 2). The relative difference between energies reconstructed with these two sets is shown in Figure 24(a) as a function of the relative ω_0 difference. A first order polynomial can be fitted with an intercept compatible with zero and a slope around 0.05, reflecting the energy bias for a given ω_0 uncertainty. This is in good agreement with [1], which reported a $\sim 0.05\%$ amplitude variation for a 1% ω_0 variation in the barrel. In the end-cap, even with a maximum 15% uncertainty on ω_0, the related systematic uncertainty on the energy is quite low, of the order of 0.5%.

Cosmic data can be used to try to discriminate between both sets of OFC for the end-caps and choose the more suited one. To achieve this goal, the pulse shape quality estimator χ^2/A^2_{max} (section 4.2.2) is computed for the two sets of OFC calculated with two different ω_0 values in S2. Results are shown for both sets in Figure 24(b) as a function of the energy. No significant differences are found within the available statistics, which is too low to perform a η-dependent analysis. The inter-calibration coefficients extracted with electrons from Z decay [22] will be mandatory to absorb the uncertainties on ω_0 and reduce the related systematic error on the energy to less than 0.2%.

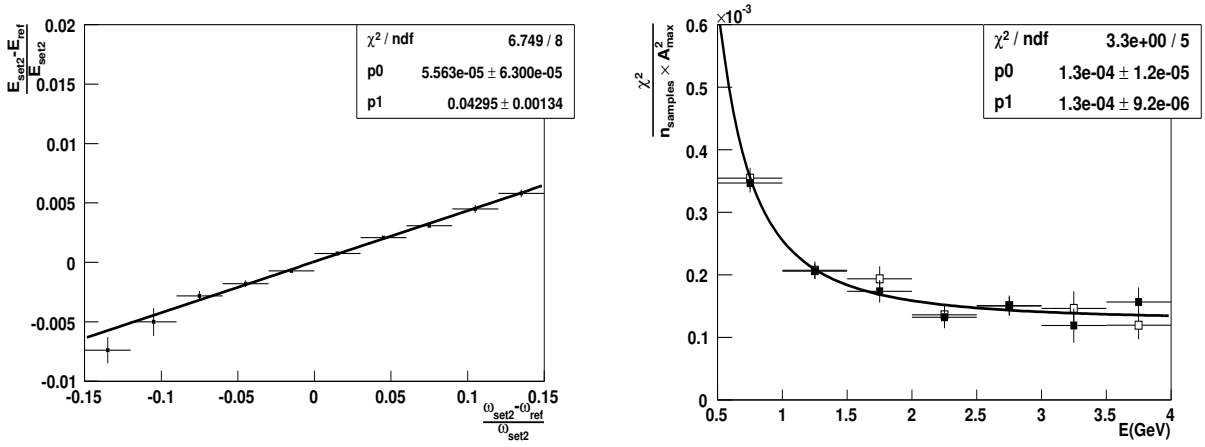

(a) (b)

Figure 24: *(Left): relative difference between energies reconstructed with the two sets of optimal filtering coefficients, as a function of the relative difference between their input resonance frequencies. A linear fit is superimposed. (Right): Estimator $\chi^2/{A_{max}}^2$ of the quality of the predicted physics pulse shapes for S2 in the end-cap, as a function of the energy, for the two sets of optimal filtering coefficients (closed symbols for reference set and open symbols for set 2). The fit is performed on the data from the second set using Equation (6).*

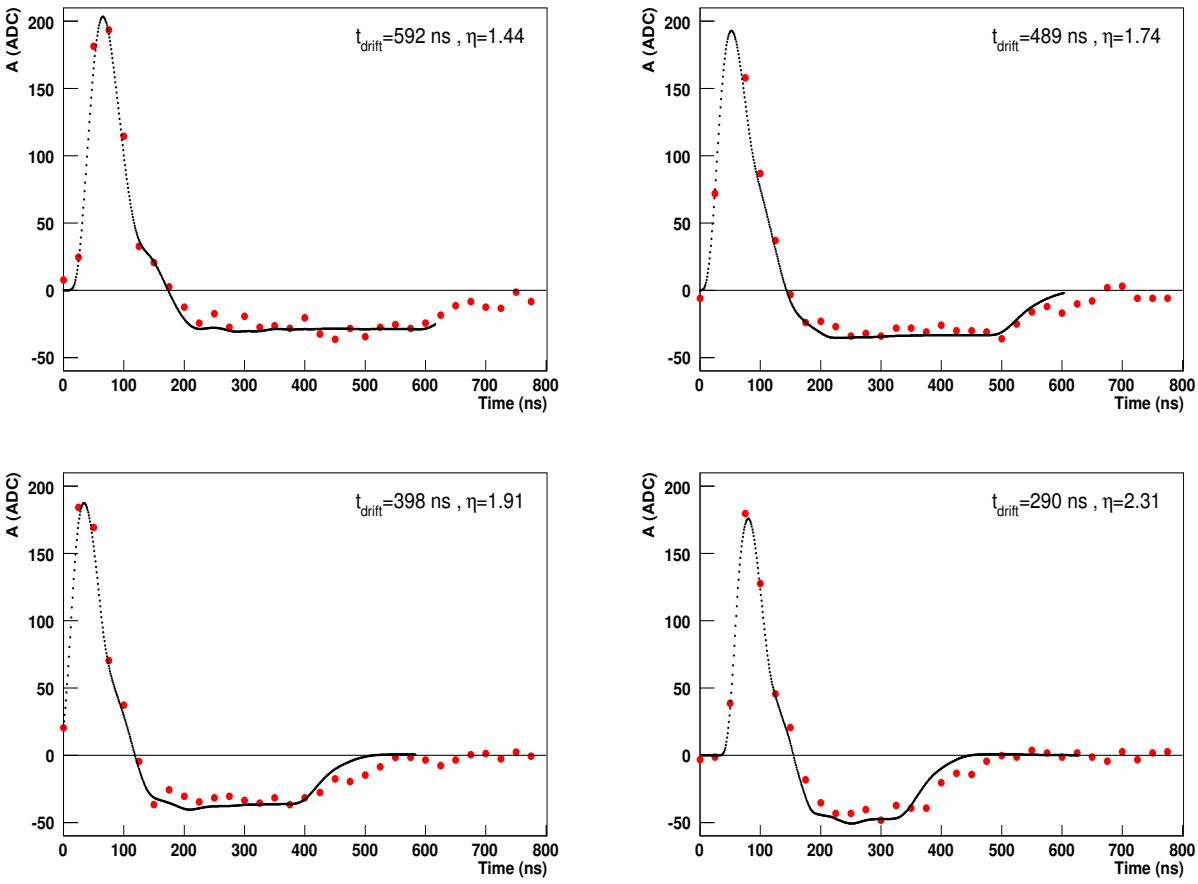

Figure 25: *Typical S2 cell responses in high gain to high energy deposits in the end-cap at different* η *values. The black curves correspond to the predicted pulse shapes using 25 samples. For each* η*, the ion drift time, reflected in the undershoot duration, is indicated.*

4.2.4 Influence of the ion drift time on the pulse shape description

The previous sections focused on the quality of the pulse shape prediction with 5 samples, that will be used to reconstruct the energy in ATLAS. The inspection of the pulse part between the 5^{th} and the 25^{th} samples, including the negative undershoot, allows to go one step further, as it permits to investigate in more detail the quality of the input parameters needed to predict the shape. For instance, the undershoot duration is directly linked to the drift time. This is illustrated in Figure 25, where typical cell responses are superimposed to the 25 samples predicted pulse shapes. For increasing η, the reduction of the undershoot duration due to the steep decrease of the ion drift time (Figure 4) is clearly visible.

As a consequence, the description of the part of the pulse shape after the 5^{th} sample is more difficult, especially in the end-cap. This is also clearly seen in Figure 25, where the undershoot prediction is systematically slightly below the data. This induces a bias on the amplitude reconstruction when a large number of samples is used [18]. To quantify this bias, Figure 26 (left) shows the relative difference between energies reconstructed with 25 or 5 samples in the barrel (open symbols) and in the end-cap (closed symbols). As expected, the bias is independent on the energy. It is around -3% in the barrel, in good agreement with what has already been reported in [5]. This is almost double in the end-cap, reflecting the difficulty to keep completely under control the steep variations of the signal reconstruction input parameters over the η-coverage (section 3). This is also seen in Figure 26 (right) that shows the same bias as a function of η. Flat in the barrel, as expected, the bias is reduced for increasing η in the end-cap outer and inner wheels. This reflects the decrease of the undershoot duration, which lowers its impact on the reconstructed energy.

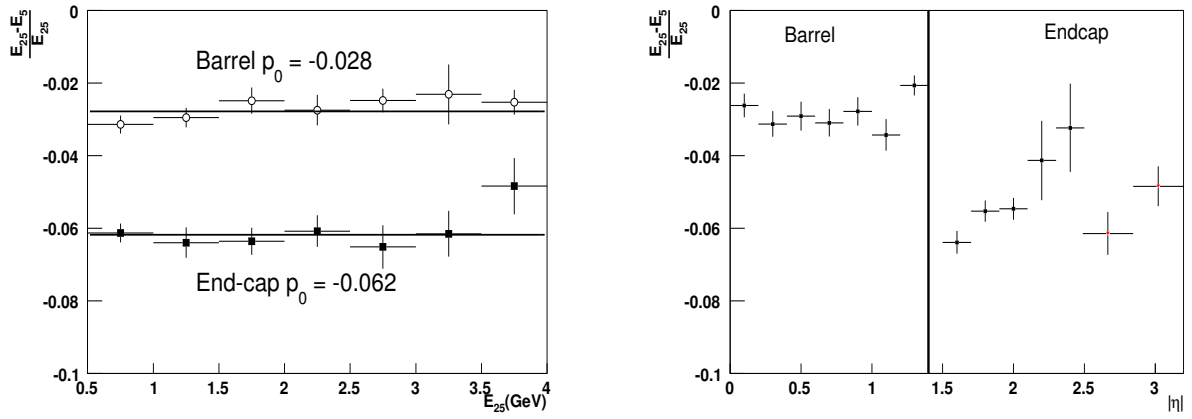

Figure 26: *Relative energy difference between reconstruction with 25 and 5 samples in S2 as a function of the energy reconstructed with 25 samples (left) and as a function of* η *(right). In the left plot, open (closed) symbols represent barrel (end-cap), and* p_0 *is the result of a fit with a constant value.*

As discussed above, a precise determination of the drift time variation along η could improve the pulse shape description between the 5^{th} and the 25^{th} samples. In the end-cap, the previous measurements were obtained by fitting 125 ns physics pulse shapes in electron beam tests with a $\sim 10\%$ precision (section 3.1.3). It is therefore interesting to extract the drift time from cosmic data looking at the 800 ns shapes. This can be done either by measuring the undershoot duration, or its relative height amplitude.

The undershoot duration is estimated by computing the difference between the time of the first sample with negative amplitude (or the sample with absolute amplitude below -2σ of the noise) and the first sample with positive amplitude after the undershoot (or the sample with absolute amplitude above -2σ of the noise). The latter may not exist for cells with high drift

[18] By construction, positive and negative areas of the pulse are equal.

time values or for predictions with 25 samples (see Figure 21), and 32 samples are therefore used for this exercise. However, the measurements with data are spoiled by the low statistics of events with high enough energies and the associated time jitter, preventing an accurate determination of the drift time. The latter can also be correlated to the relative height amplitude of the undershoot r :

$$r = \frac{A_{max}^{OFC_{5s}} + |\frac{1}{n}\sum_{i=1}^{n} A_{min}^{i}|}{A_{max}^{OFC_{5s}}} \tag{7}$$

where $n = 5$ is the number of samples used to estimate the average of the undershoot height [19]. Figure 27 shows r as a function of the input drift time in the end-cap and in the barrel, as obtained with data and with the predicted physics pulse shapes. The barrel r value is higher than for the end-cap, reflecting the shape difference in the falling edge (between the 5th and the 9th samples) observed in Figure 21, which is linked to different capacitance values and signal cable lengths. In the end-cap, a linear behaviour between r and the input drift time is observed, both for data and predictions. Data derived r values are systematically lower than those from the pulse shape prediction. This suggests that the input drift time has been systematically underestimated, as already inferred from Figure 25. However, the statistics is too poor to deconvolute all second order effects (electric field variation with η, LC dependence, non-projectivity of energy deposits, ...) and extract an enough accurate measurement usable for the signal reconstruction.

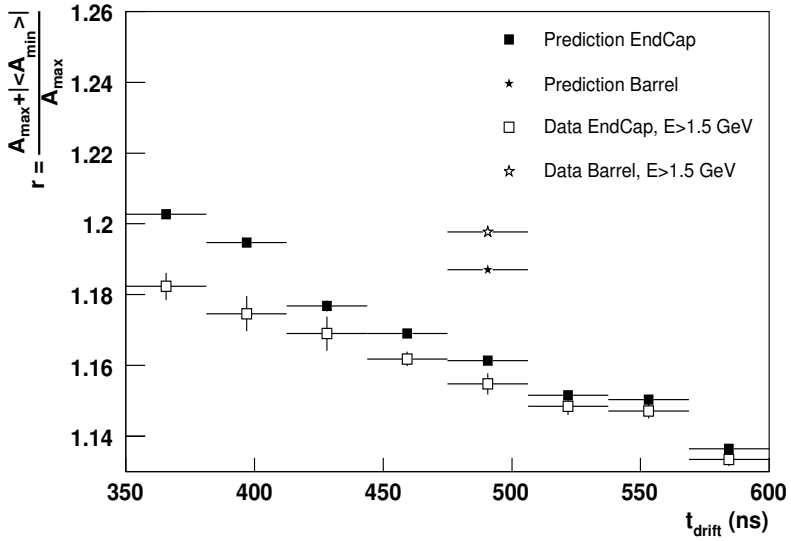

Figure 27: *Relative height amplitude of the undershoot r (see text) as a function of the input drift time in S2 for the barrel and the end-cap. Values derived from data and from predicted physics pulse shapes are shown. To lower the noise contribution, an energy cut $E > 1$ GeV is applied.*

[19] The sample A_{min}^{1} is located 50 ns after the first sample with negative amplitude.

5 Conclusions

Because of a complicated geometry, the signal reconstruction in the end-caps of the electromagnetic calorimeter is more challenging than in the barrel. In this note, all input ingredients (except the ion drift time) of the method foreseen in ATLAS have been derived *in situ* from calibration data in the three end-cap layers, and compared to direct measurements. They have been compared extensively to the barrel ones, which can be taken as a reference, as most of its parameters vary very weakly along η and have been precisely measured. This allowed to spot and solve some problems, and assess the coherence of the signal reconstruction over the complete calorimeter coverage.

The next step was to test this signal reconstruction, and before LHC start cosmic muons are the only data that can be used. The non-projective situation of the end-caps with respect to such events prevents the use of the muon ionisation energy deposit. However, the selection of the few % of events with catastrophic high energy deposits (typically $E > 500$ MeV) is particularly suitable to perform an *in situ* test of the signal reconstruction. Moreover, this can be done in a coherent way over the entire calorimeter coverage, $0 < \eta < 3.2$, which represents the first attempt to unify barrel and end-cap *in situ* data in a common analysis.

Even with the limited available statistics, a systematic and quantitative comparison between data and predicted physics pulse shapes has been performed for the three layers of the EM calorimeter. Results are similar in the barrel and the end-cap, only slightly worse for the latter as expected from its more complex geometry. This is the first proof of the quality of an ATLAS-like signal reconstruction in the end-caps, despite its challenging aspect, and gives confidence that the energy reconstruction is in good control over the complete calorimeter coverage $0 < \eta < 3.2$. This could be a real asset for an early discovery in electron or photon channel.

Even if this study could be extended to a systematic search for problematic cells with more statistics, using the latest M5 and M6 muon week data, high p_T isolated electrons from LHC data will be mandatory for a refined check of the physics pulse shapes in all channels [27], which will be needed to reach the ultimate performance.

Acknowledgements

We warmly thank our colleague M. Delmastro for fruitful discussions, help and careful reading of the note. We also thank E. Monnier, M. Aleksa and W. Lampl for their constant help and support. The present analysis would not have been possible without the dedicated effort of many people in our LAr detector group and the ATLAS collaboration over many years. We are especially indebted to those who built, integrated and installed the LAr detector in the ATLAS cavern, and those who operate the detector on a daily basis.

References

[1] D. Banfi, M. Delmastro and M. Fanti, *Cell response equalization of the ATLAS electromagnetic calorimeter without the direct knowledge of the ionization signals*, SN-ATLAS-2005-054, J. Inst **1** (2006) P08001.

[2] M. Aharrouche *et al.*, *Energy linearity and resolution of the ATLAS electromagnetic barrel calorimeter in an electron test-beam*, Nucl. Inst. Meth. **A 568** (2006) 601.

[3] J. Colas *et al.*, *Response Uniformity of the ATLAS Liquid Argon Electromagnetic Calorimeter*, Nucl. Inst. Meth. **A 582** (2007) 429, arXiv:0709.1094 [physics].

[4] M. Aleksa *et al.*, *ATLAS Combined Testbeam : Computation and Validation of the Electronic Calibration Constants for the Electromagnetic Calorimeter*, ATLAS note ATL-LARG-PUB-2006-003.
D. Goldin and M. Delmastro, *On the feasibility of predicting the ATLAS EM Calorimeter ionization signals using the Time Convolution Method at the LHC sampling rate*, ATLAS note ATL-LARG-PUB-2007-004.

[5] M. Cooke, P.S. Mangeard, M. Plamondon *et al.*, *In situ commissioning of the ATLAS electromagnetic calorimeter with cosmic muons*, ATLAS note ATL-LARG-PUB-2007-013.

[6] The ATLAS Collaboration, *Liquid Argon Calorimeter, Technical Design Report*, CERN/LHCC/96-41.

[7] B. Aubert *et al.*, *Construction, assembly and tests of the ATLAS electromagnetic barrel calorimeter*, Nucl. Inst. Meth. **A 558** (2006) 388.

[8] M. Aleksa *et al.*, *Construction, assembly and tests of the ATLAS electromagnetic end-cap calorimeter*, submitted to J. Inst.

[9] W.E. Cleland and E.G. Stern, *Signal processing considerations for liquid ionization calorimeter in a high rate environment*, Nucl. Inst. Meth. **A 338** (1994) 467.

[10] C. Collard *et al.*, *Prediction of signal amplitude and shape for the ATLAS electromagnetic calorimeter*, ATLAS note ATL-LARG-PUB-2007-010.

[11] F. Hubaut *et al.*, *Crosstalk in production modules of the Electromagnetic Endcap Calorimeter*, ATLAS note ATL-LARG-2003-012.

[12] S. Baffioni *et al.*, *Electrical Measurements on the ATLAS electromagnetic barrel calorimeter*, ATLAS note ATL-LARG-PUB-2007-005.

[13] Lydia Fayard, *Hardware measurements of Rcal and LC in barrel*, presentation at EM calibration workshop, Annecy, october 2007.

[14] J. Colas, *Calibration and non ideal calibration cables*, presentation at EM electronics calibration meeting, LAr Week, May 2007.

[15] C. de La Taille and L. Serin *Temperature dependance of the ATLAS electromagnetic calorimeter signal. Preliminary drift time measurement*, ATLAS note LARG-NO-29.

[16] B. Aubert *et al.*, *Performance of the ATLAS Electromagnetic Calorimeter Endcap Module 0*, Nucl. Inst. Meth. **A 500** (2003) 178.

[17] F. Hubaut and C. Serfon, *Response uniformity of the ATLAS electromagnetic endcap calorimeter*, ATLAS note ATL-LARG-2004-015.

[18] C. Oliver and J. del Peso, *Outer Wheel Uniformity of the Electromagnetic EndCap Calorimeter*, ATLAS note ATL-LARG-PUB-2005-002.

[19] P. Barrillon et al., *Electrical tests for the validation of the electromagnetic end-cap calorimeter modules*, ATLAS note ATL-LARG-2003-004.

[20] Marco Delmastro, *How to compute optimal filtering coefficients*, presentation at EM calibration workshop, Annecy, October 2007.

[21] Lydia Fayard, *Comparison between different ionisation pulse predictions*, presentation at EM electronics calibration meeting, LAr Week, November 2005.

[22] F. Djama, *Using $Z^0 \rightarrow e^+e^-$ for Electromagnetic Calorimeter Calibration* , ATLAS note ATLAS-2004-008.

[23] C. Gabaldon, *Check OFC using Pedestal runs* , presentation at BP3C meeting, 30/08/2007.

[24] K. Anderson *et al.*, *Stand-alone Cosmic Ray Trigger Electronics for the ATLAS Tile Calorimeter*, Proceedings, 10th Workshop on Electronics for LHC and Future Experiments, September 13-17, 2004, Boston, USA.

[25] W. Lampl *et al.*, *Digitization of LAr calorimeter for CSC simulations*, ATLAS note ATL-LARG-PUB-2007-011.

[26] J. Ban *et al.*, *ATLAS liquid argon calorimeter back end electronics*, J. Inst **2** (2007) P06002.

[27] Marco Delmastro, *Quality factor analysis and digital filtering optimization*, presentation at EM electronics calibration meeting, LAr Week, December 2007.

Appendix 1: EM calorimeter description

The electromagnetic calorimeter granularity is detailed in Table 4. The High-Voltage sector definitions, consequence of the end-cap geometry, is given in Table 5.

		Front (S1)	Middle (S2)	Back (S3)
Barrel	$\|\eta\| \leq 1.35$	$0.025/8 \times 0.1$	0.025×0.025	0.050×0.025
	$1.35 \leq \|\eta\| \leq 1.4$	$0.025/8 \times 0.1$	0.025×0.025	–
	$1.4 \leq \|\eta\| \leq 1.475$	0.025×0.025	0.075×0.025	–
End-caps	$1.375 \leq \|\eta\| \leq 1.425$	0.050×0.1	0.050×0.025	–
	$1.425 \leq \|\eta\| \leq 1.5$	0.025×0.1	0.025×0.025	–
	$1.5 \leq \|\eta\| \leq 1.8$	$0.025/8 \times 0.1$	0.025×0.025	0.050×0.025
	$1.8 \leq \|\eta\| \leq 2.0$	$0.025/6 \times 0.1$	0.025×0.025	0.050×0.025
	$2.0 \leq \|\eta\| \leq 2.4$	$0.025/4 \times 0.1$	0.025×0.025	0.050×0.025
	$2.4 \leq \|\eta\| \leq 2.5$	0.025×0.1	0.025×0.025	0.050×0.025
	$2.5 \leq \|\eta\| \leq 3.2$	–	0.1×0.1	0.1×0.1

Table 4: *Granularity* $\Delta\eta \times \Delta\phi$ *for each calorimeter sampling (Front, Middle and Back).*

	Barrel	End-cap outer wheel						
HV region	0	1	2	3	4	5	6	7
η range	0-1.475	1.375-1.5	1.5-1.6	1.6-1.8	1.8-2.0	2.0-2.1	2.1-2.3	2.3-2.5
HV values	2000 V	2500 V	2300 V	2100 V	1700 V	1500 V	1250 V	1000 V

Table 5: *The high voltage regions of the barrel and end-cap outer wheel EM calorimeter.*